Active Harmonic Filtering with Selective Overcurrent Limitation for Grid-Forming VSCs: Stability Analysis and Experimental Validation

Francisco Jesús Matas-Díaz, Manuel Barragán-Villarejo, José María Maza-Ortega, *Member, IEEE,* Georgios C. Kryonidis, *Senior Member, IEEE,* Kyriaki-Nefeli Malamaki, *Member, IEEE,* Charis S. Demoulias, *Senior Member, IEEE*

***Abstract*—The high penetration of renewable energy sources (RES) interfaced with power electronics together with new non-linear loads pose new challenges in the grid operation. In fact, power systems with reduced inertia and high harmonic distortion will be common in a near future. Recently, the grid-forming operation of voltage source converters (VSCs) has emerged to address these challenges, mimicking the contribution of synchronous generators to the system inertia. In addition, these grid-connected VSCs can be used at the same time for reducing the harmonic distortion by applying active filtering techniques. However, these harmonic compensation algorithms can generate VSC overloading. This paper proposes a method for dynamically adjusting the individual virtual impedance of the filtered harmonics to prevent the power converter overcurrent. For this purpose, the value of each harmonic virtual impedance is modified according to a priority which can be set by the final user according to the established power quality standard. The paper includes a theoretical stability analysis of the controller and experimental results to validate the proposed algorithm.**

***Index Terms*—Power quality, converter interfaced generators, active harmonic mitigation, renewable energy sources, grid-forming inverters, stability analysis, overcurrent protection.**

I. Introduction

The future of power generation will be dominated by renewable energy sources (RES). In this way, the conventional synchronous generators will be replaced with RES power plants which will be connected to the grid using converter interfaced generators (CIGs). This scenario may lead to new technical challenges, where larger frequency and voltage deviations are expected due to the reduced system inertia [1], affecting the secure and reliable operation of the power system [2]. This change comes along with a transition in the demand side, where traditional electro-mechanical loads are being replaced by power electronics such as variable speed drives, power supplies or lighting devices. These non-linear loads improve the performance, efficiency and flexibility but, at the same time, introduce harmonic currents. This has a negative effect on the distribution system causing, among others, distorted nodal voltages [3] and transformer overheating [4]. The impact on the power quality is particularly high in low voltage networks and microgrids, where the penetration of non-linear loads is steadily increasing within industrial, commercial and domestic consumers [5].

With this regard, CIGs based on voltage source converters (VSCs) composed of switched devices such as insulated-gate bipolar transistors (IGBTs) may contribute to address these new challenges due to the inherent flexibility provided by their control algorithms.

On the one hand, regarding the reduced inertia of modern power systems, grid-forming operation of CIGs has recently emerged to support and control the system frequency and voltage [6]. For doing so, it is required to either operate below the RES maximum power point or include an energy storage system [7]. Several ways to implement the grid-forming mode can be found in the specialized literature [8]: droop controllers for active and reactive power sharing [9], advanced algorithms mimicking the dynamic performance of a synchronous generator [10] or virtual oscillators [11]. All of them provide frequency and voltage control and they can operate in both islanded and grid-connected systems. This is because they do not require a phase-locked loop (PLL) or other frequency estimation method to synchronize with the system they are connected to. In general, the control structure of a grid-forming VSC consists of a hierarchical controller composed of an outer and an inner control loop, OCL and ICL respectively [12]. The OCL is in charge of the synchronization and the computation of the frequency and voltage references for the ICL. Meanwhile, the ICL can be implemented in different ways: open loop [13], single current controller [14], [15], single voltage controller [16] and cascade voltage and current controllers [17]. The main drawback of the three first algorithms is the lack of controllability of the capacitor voltage and/or inductor current which is critical in abnormal operation conditions with a fast dynamics such as short-circuit faults. With this regard, the use of cascade controllers guarantees that the VSC voltage and current remain within the technical limits. This approach, however, is extremely sensitive to the characteristics of the Point of Interconnection (POI), i.e. short-circuit power and R/X ratio [8]. In addition, the voltage control loop may become unstable because of the feedforward terms of the current controller [18]. This drawback can be

Manuscript received XXXX. (Corresponding author: manuelbarragan@us.es.)

Francisco Jesús Matas-Díaz, Manuel Barragán-Villarejo and José María Maza-Ortega are with the Department of Electrical Engineering, Universidad de Sevilla, 41004 Sevilla, Spain (e-mail: fmatas@us.es; manuelbarragan@us.es; jmmaza@us.es).

Georgios C. Kryonidis, Kyriaki-Nefeli D. Malamaki, and Charis S. Demoulias are with the Department of Electrical & Computer Engineering, Aristotle University of Thessaloniki, 54124 Thessaloniki, Greece (e-mail: kyriaki_nefeli@hotmail.com; kryonidi@ece.auth.gr; chdimoul@auth.gr).

Citation Information: DOI: 10.1109/TIA.2024.3369595

overcome using an ICL based just on a current controller. In this case, the voltage control is included within the OCL through primary and secondary control loops [19]. Evidently, this voltage control has a slower dynamic response than those strategies with a voltage control within the ICL, but enough to maintain the voltages within technical limits under normal operation conditions. Moreover, these controllers are also able to limit the VSC current in case of short-circuit faults [20], [21].

On the other hand, with respect to the harmonic mitigation, passive filters [22], active power filters [23] or hybrid filters can be installed nearby large non-linear loads at the cost of additional investments. Alternatively, CIGs with proper control actions may help to reduce the harmonic distortion [24]. A set of resonant controllers tuned to the targeted harmonics can be added to the ICL either in the current or voltage control loop. In the first case, the harmonic current reference is computed using a virtual harmonic admittance and the POI harmonic voltage [25]. This virtual harmonic admittance is dynamically modified until the reference harmonic voltage is reached, as long as the VSC rated current is not exceed. This is an indirect method of harmonic voltage compensation since the virtual admittance is modified following a *trial and error* process. For this reason, this methodology is not suitable in case of rapidly time-varying non-linear loads. As an alternative, the harmonic compensation can be integrated in the ICL voltage control loop by adding to the fundamental frequency controller a set of cascade resonant controllers tuned at the targeted harmonics [26], [27]. In this way, any harmonic voltage reference can be directly tracked. The harmonic voltage references can be computed using a virtual impedance approach to improve the power sharing and the selective voltage harmonic compensation [28]. Independently of the implemented harmonic controller, the system harmonic stability needs to be ensured. For doing so, different approaches have been previously proposed ranging from simplified Norton-based impedance model [29] to sophisticated ones based on state-space models [30]. The selection of the stability analysis tool depends on several factors: available information, main goal of the analysis (design-oriented process, identification of dynamic modes, participation factors, modularity, scalability, computational effort, etc.). A comprehensive overview of this topic with the pros and cons of each method can be found in [31].

Nevertheless, it is still possible to improve the design process and the performance of the existing harmonic controllers. Particularly, it is required to compute the resonant controller parameters to guarantee the controller stability and an adequate tracking of the harmonic references independently of the network characteristics. Furthermore, VSC operational limits, i.e. rated current and voltage, may be reached during the provision of the active harmonic filtering (AHF) service. In the existing literature, there are several current-limiting control strategies based on whether the total output current magnitude of the grid-forming VSC is directly or indirectly controlled [32]. Basically, these are classified in three categories: (i) direct current-limiting control [33], (ii) indirect current-limiting control [34] as virtual impedance current limiter [35] and, (iii) hybrid current-limiting control [36]. Regardless of the method used to limit the current, all of them aim to limit the total current, without discriminating between the different current components of this current. With this regard, the limitation of the AHF capability in case of VSC overload has been previously explored in current controllers for active power filters: saturation approaches [37], [38], virtual impedance techniques [39] and optimization algorithms [40]. However, the limitation of the AHF capability in case of VSC overcurrent with direct harmonic voltage tracking remains unexplored.

The main objective of this paper is to provide a stable AHF functionality to grid-forming VSCs by adding a direct harmonic voltage controller with selective current limitation in case of overloading. The harmonic voltage reference is set by means of an adaptive virtual harmonic impedance which is modified to maintain the current below its rated value. Each virtual harmonic impedance can be calculated independently to reflect the relative importance of each harmonic according to the established power quality standard. The proposed strategy can be implemented at any CIG, since it does not require adding new measurement devices or hardware components. Moreover, its application is of particular interest in CIGs within low voltage networks and microgrids, where the non-linear loads may deteriorate the power quality.

Finally, it is important to highlight that this paper has the following contributions with respect to [41]:

- Evaluation of the proposed solution in grid-connected, instead of islanded, grid-forming VSCs.
- OCL based on a virtual synchronous generator (VSG) which allows the synchronization with the grid and inertial response.
- Stability analysis of the grid-forming VSC controller with AHF and selective overcurrent protection resorting to a small-signal analysis based on state-space equations.
- Computation of the virtual harmonic impedance to prevent VSC overloading according to the priority established in the EN 50160 standard [42] for each targeted harmonic.

The rest of the paper is organized as follows. Section II presents the state-space modelling of the grid-forming VSC including the system dynamics: VSG, AHF and selective overloading protection. Section III outlines a small-signal stability analysis to evaluate the influence and stability range of the controller parameters. From this analysis, the final values of the controller gains are determined. Section IV provides the experimental validation of the proposal. Finally, the paper closes with the main conclusions.

II. State-Space Modelling of the Grid-Forming VSC

This section outlines the state-space model of a grid-connected VSC providing grid-forming capability with AHF and selective overcurrent protection. The proposed control algorithm is shown in Fig. 1, where all the parameters, variables and controller gains used along paper are specified. The state-space model is composed of four main blocks analyzed in the following subsections: (i) the grid-connected VSC model,

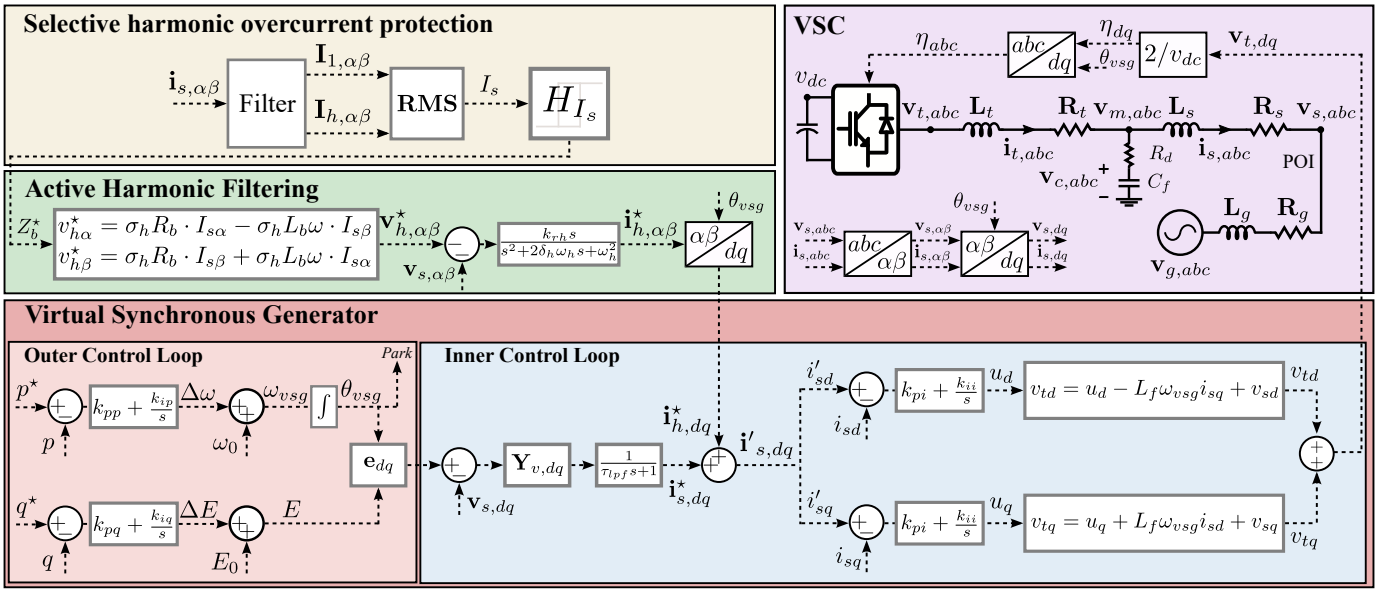

Fig. 1. Proposed controller for the grid–forming VSCs with AHF and overcurrent protection.

(ii) the main controller of the grid-forming VSC implemented through a VSG, (iii) the AHF functionality through direct harmonic voltage control, and (iv) the selective harmonic overcurrent protection.

A. Grid-Connected VSC model

The grid-connected VSC is a three-phase three-wire device connected to the grid through an LCL coupling filter, which also has a physical damping resistor incorporated in series with the capacitor. The grid is modeled as an AC voltage source with an series connected inductive impedance (R_g and L_g). The differential equations of the grid-connected VSC in the dq rotating reference frame, which is synchronized with the VSG angle, θ_{vsg}, are as follows:

$$\begin{cases} v_{td} - v_{md} = R_t i_{td} + L_t \dfrac{di_{td}}{dt} - L_t \omega_{vsg} i_{tq}, \\ v_{tq} - v_{mq} = R_t i_{tq} + L_t \dfrac{di_{tq}}{dt} + L_t \omega_{vsg} i_{td}, \end{cases} \tag{1}$$

$$\begin{cases} v_{md} - v_{sd} = R_s i_{sd} + L_s \dfrac{di_{sd}}{dt} - L_s \omega_{vsg} i_{sq}, \\ v_{mq} - v_{sq} = R_s i_{sq} + L_s \dfrac{di_{sq}}{dt} + L_s \omega_{vsg} i_{sd}, \end{cases} \tag{2}$$

$$\begin{cases} v_{md} = v_{cd} + R_d (i_{td} - i_{sd}), \\ v_{mq} = v_{cq} + R_d (i_{tq} - i_{sq}), \end{cases} \tag{3}$$

$$\begin{cases} C_f \dfrac{dv_{cd}}{dt} - C_f \omega_{vsg} v_{cq} = (i_{td} - i_{sd}), \\ C_f \dfrac{dv_{cq}}{dt} + C_f \omega_{vsg} v_{cd} = (i_{tq} - i_{sq}), \end{cases} \tag{4}$$

$$\begin{cases} v_{sd} - v_{gd} = R_g i_{sd} + L_g \dfrac{di_{sd}}{dt} - L_g \omega_{vsg} i_{sq}, \\ v_{sq} - v_{gq} = R_g i_{sq} + L_g \dfrac{di_{sq}}{dt} + L_g \omega_{vsg} i_{sd}, \end{cases} \tag{5}$$

where L_t and L_s are the inverter-side and the grid-side filter inductances respectively, R_t and R_s are their corresponding resistances, C_f is the filter capacitance, R_d is the damping resistance, $\mathbf{v}_{t,dq} = [v_{td}, v_{tq}]$ is the voltage at the VSC terminals, $\mathbf{v}_{m,dq} = [v_{md}, v_{mq}]$ is the voltage across the capacitor and damping resistor, $\mathbf{v}_{c,dq} = [v_{cd}, v_{cq}]$ is the capacitor voltage, $\mathbf{v}_{s,dq} = [v_{sd}, v_{sq}]$ is the POI voltage, $\mathbf{v}_{g,dq} = [v_{gd}, v_{gq}]$ is the source voltage of the grid, $\mathbf{i}_{t,dq} = [i_{td}, i_{tq}]$ is the inverter-side inductor current, $\mathbf{i}_{s,dq} = [i_{sd}, i_{sq}]$ is the grid-side inductor current, and ω_{vsg} is the VSG angular frequency.

Considering the equations above, the model of the grid-connected VSC adds six state variables $\mathbf{x_f}$ to the state-space equations:

$$\mathbf{x_f} = [i_{td}, i_{tq}, i_{sd}, i_{sq}, v_{cd}, v_{cq}]. \tag{6}$$

B. Virtual Synchronous Generator

The selected VSG model for providing grid-forming capability is the one presented in [15], which is composed of an OCL and an ICL.

The OCL consists of two parallel proportional-integral (PI) controllers for the active and reactive power, as shown in Fig. 1. The active power controller enables the synchronization with the grid by modifying the virtual rotor angle, θ_{vsg}. The reactive power controller computes the amplitude of the virtual electromotive force, E. Therefore, the OCL equations are the following:

$$\begin{cases} \omega_{vsg} = k_{pp} \dfrac{d\xi_p}{dt} + k_{ip} \xi_p + \omega_0, \\ \dfrac{d\theta_{vsg}}{dt} = \omega_{vsg}, \\ \dfrac{d\xi_p}{dt} = p^* - p, \end{cases} \tag{7}$$

$$\begin{cases} E = k_{pq} \dfrac{d\xi_q}{dt} + k_{iq} \xi_q + E_0, \\ \dfrac{d\xi_q}{dt} = q^* - q, \end{cases} \tag{8}$$

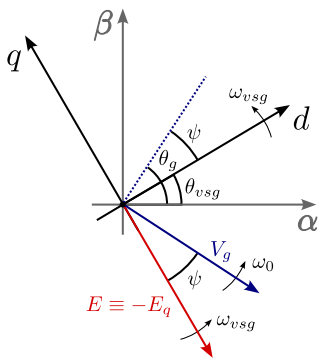

Fig. 2. Grid voltage VSG electromotive force in the $\alpha\beta$ and dq frames.

where ξ_p is the integral of the active power error, p is the POI active power, $p^\star$ is the reference active power, ω_0 is the rated frequency, k_{pp} and k_{ip} are the proportional and integral gains of the PI active power controller, ξ_q is the integral of the reactive power error, q is the POI reactive power, $q^\star$ is the reference reactive power, E_0 is the rated electromotive force, and k_{pq} and k_{iq} are the proportional and integral gains of the PI reactive power controller.

The POI active and reactive powers, p and q, are calculated in dq axes as:

$$\begin{cases} p = \dfrac{3}{2}(v_{sd}i_{sd} + v_{sq}i_{sq}), \\ q = \dfrac{3}{2}(v_{sq}i_{sd} - v_{sd}i_{sq}). \end{cases} \tag{9}$$

The electromotive force lies along the q axis as shown in Fig. 2. This leads to an electromotive force in the dq coordinates always equal to $\mathbf{e}_{dq} = [0, -E]$. On the other hand, it is considered that the grid voltage rotates at the nominal frequency, ω_0. This means that the grid voltage is considered a perturbation not adding any dynamic to the system [43]. Therefore, it can be defined a phase shift, ψ, between the grid voltage and the electromotive force, as shown in Fig. 2, which evolves according to the VSG angle dynamics:

$$\begin{cases} \psi = \theta_g - \theta_{vsg}, \\ \dfrac{d\psi}{dt} = \omega_0 - \dfrac{d\theta_{vsg}}{dt}. \end{cases} \tag{10}$$

This approach allows to replace θ_{vsg} by ψ in (7), maintaining the VSG dynamics but adding the grid angular frequency ω_0 in the model.

The ICL consists of a single PI current controller implemented in dq coordinates. The current references are obtained from the electromotive force, $\mathbf{e}_{dq}$, the POI voltage, $\mathbf{v}_{s,dq}$, and a virtual admittance, $Y_v = G_v - jB_v$. Additionally, a low-pass filter (LPF) is applied to these reference currents before introducing them into the current controller with the aim of providing references with the lowest possible harmonic content. The current references, i_{sd}^{vsg} and i_{sq}^{vsg}, can be formulated as follows:

$$\begin{cases} i_{sd}^{vsg} = G_v(e_d - v_{sd}) + B_v(e_q - v_{sq}), \\ i_{sq}^{vsg} = -B_v(e_d - v_{sd}) + G_v(e_q - v_{sq}), \end{cases} \tag{11}$$

$$\begin{cases} i_{sd}^{vsg} = \tau_{lpf}\dfrac{di_{sd}^\star}{dt} + i_{sd}^\star, \\ i_{sq}^{vsg} = \tau_{lpf}\dfrac{di_{sq}^\star}{dt} + i_{sq}^\star, \end{cases} \tag{12}$$

where τ_{lpf} is the LPF time constant and $\mathbf{i}_{s,dq}^\star = [i_{sd}^\star, i_{sq}^\star]$ is filtered reference current.

Finally, the PI current controller equations, including the cross-coupling cancellation and feed-forward terms are:

$$\begin{cases} v_{td} = k_{pi}\dfrac{d\xi_{id}}{dt} + k_{ii}\xi_{id} - (L_t + L_s)\omega_{vsg}i_{sq} + v_{sd}, \\ v_{tq} = k_{pi}\dfrac{d\xi_{iq}}{dt} + k_{ii}\xi_{iq} + (L_t + L_s)\omega_{vsg}i_{sd} + v_{sq}, \\ \dfrac{d\xi_{id}}{dt} = i_{sd}^\star - i_{sd}, \\ \dfrac{d\xi_{iq}}{dt} = i_{sq}^\star - i_{sq}, \end{cases} \tag{13}$$

where ξ_{id} and ξ_{iq} are the integral of the current errors in dq axis and k_{pi} and k_{ii} are the proportional and integral gains of the PI current controller respectively.

Considering (7)-(13), the model of the VSG control loops adds seven new state variables to the state-space equations:

$$\mathbf{x}_{vsg} = [\psi, \xi_p, \xi_q, i_{sd}^\star, i_{sq}^\star, \xi_{id}, \xi_{iq}]. \tag{14}$$

C. Active Harmonic Filtering

The harmonic voltage control is provided by including a set of resonant controllers to each of the targeted harmonics. The objective is to track a harmonic voltage reference in the $\alpha\beta$ domain, $\mathbf{v}_{h,\alpha\beta}^\star = [v_{h\alpha}^\star, v_{h\beta}^\star]$, which corresponds to the required POI harmonic voltage. Note that the resonant controllers are implemented in the $\alpha\beta$ coordinates, rather than in the dq frame, since it is necessary to compensate each harmonic in its corresponding sequence. These resonant controllers generate a new current reference, $\mathbf{i}_{h,\alpha\beta}^\star = [i_{h\alpha}^\star, i_{h\beta}^\star]$, which is converted to the dq-axes before being added to the VSG fundamental reference current (13), as shown in Fig. 1.

The resonant controllers in the $\alpha\beta$ reference frame can be formulated in the Laplace domain as:

$$\begin{cases} \dfrac{i_{h\alpha}^\star(s)}{\epsilon_{h\alpha}(s)} = \dfrac{k_{rh}s}{s^2 + 2\delta_h\omega_h s + \omega_h^2}, \\ \dfrac{i_{h\beta}^\star(s)}{\epsilon_{h\beta}(s)} = \dfrac{k_{rh}s}{s^2 + 2\delta_h\omega_h s + \omega_h^2}, \\ \epsilon_{h\alpha}(s) = v_{h\alpha}^\star(s) - v_{s\alpha}(s), \\ \epsilon_{h\beta}(s) = v_{h\beta}^\star(s) - v_{s\beta}(s), \end{cases} \tag{15}$$

where $\epsilon_{h,\alpha\beta} = [\epsilon_{h\alpha}, \epsilon_{h\beta}]$ is the harmonic voltage error, $\mathbf{v}_{s,\alpha\beta} = [v_{s\alpha}, v_{s\beta}]$ is the POI harmonic voltage while k_{rh}, δ_h and ω_h are the gain, damping and tuned harmonic frequency of the *h-th* resonant controller. However, it is required to transform (15) to the dq coordinates, where the grid-connected VSC and VSG models have been derived:

$$\begin{cases} \dfrac{i_{hd}^\star(s)}{\epsilon_{hd}(s)} = \dfrac{k_{rh}(s + j\omega_{vsg})}{(s + j\omega_{vsg})^2 + 2\delta_h\omega_h(s + j\omega_{vsg}) + \omega_h^2}, \\ \dfrac{i_{hq}^\star(s)}{\epsilon_{hq}(s)} = \dfrac{k_{rh}(s + j\omega_{vsg})}{(s + j\omega_{vsg})^2 + 2\delta_h\omega_h(s + j\omega_{vsg}) + \omega_h^2}, \\ \epsilon_{hd}(s) = v_{hd}^\star(s) - v_{sd}(s), \\ \epsilon_{hq}(s) = v_{hq}^\star(s) - v_{sq}(s), \end{cases} \tag{16}$$

where $\epsilon_{h,dq} = [\epsilon_{hd}, \epsilon_{hq}]$ is the harmonic voltage error, $\mathbf{i}^{\star}_{h,dq} = [i^{\star}_{hd}, i^{\star}_{hq}]$ is the reference harmonic current and $\mathbf{v}^{\star}_{h,dq} = [v^{\star}_{hd}, v^{\star}_{hq}]$ is the reference harmonic voltage. Finally, the time-domain formulation of (16) is as follows:

$$\begin{cases} \dfrac{di^{\star}_{hd}}{dt} = k_{rh}\epsilon_{hd} - (2\delta_h\omega_h + j\omega_{vsg})i^{\star}_{h,d} - \omega_h^2\gamma_{hd}, \\ \dfrac{di^{\star}_{hq}}{dt} = k_{rh}\epsilon_{hq} - (2\delta_h\omega_h + j\omega_{vsg})i^{\star}_{hq} - \omega_h^2\gamma_{hq}, \end{cases} \tag{17}$$

$$\begin{cases} \dfrac{d\gamma_{hd}}{dt} = i^{\star}_{hd} - j\omega_{vsg}\gamma_{hd}, \\ \dfrac{d\gamma_{hq}}{dt} = i^{\star}_{hq} - j\omega_{vsg}\gamma_{hq}, \end{cases} \tag{18}$$

where $\gamma_{h,dq} = [\gamma_{hd}, \gamma_{hq}]$ is a new state variable representing the integral of $\mathbf{i}^{\star}_{h,\alpha\beta}$ in the dq reference frame: $\gamma_{h,dq}(s) = (sj\omega_{vsg})^{-1}\mathbf{i}^{\star}_{h,dq}(s)$.

The reference harmonic currents $\mathbf{i}^{\star}_{h,dq}$ are added to the previously computed VSG reference current, $\mathbf{i}'_{dq} = \mathbf{i}^{\star}_{s,dq} + \mathbf{i}^{\star}_{h,dq}$, which is the input of the PI current controller. Therefore, (13) is reformulated as:

$$\begin{cases} \dfrac{d\xi_{id}}{dt} = i'_{sd} - i_{sd}, \\ \dfrac{d\xi_{iq}}{dt} = i'_{sq} - i_{sq}. \end{cases} \tag{19}$$

Note that the perfect tracking of the reference harmonic currents $\mathbf{i}^{\star}_{h,dq}$ requires the use of resonant controllers tuned for each harmonic, like the ones used for the harmonic voltages. However, it is also possible to apply just a regular PI controller which, along with the resonant voltage controllers, provides a high bandwith to track the reference harmonic currents. In this manner, the computational cost of the AHF functionality is considerably reduced.

The harmonic voltage control introduces four new differential equations (17)-(18) per each targeted harmonic h and their corresponding state variables:

$$\mathbf{x}_h = [i^{\star}_{hd}, i^{\star}_{hq}, \gamma_{hd}, \gamma_{hq}]. \tag{20}$$

The performance analysis of the AHF can be alternatively evaluated through a simplified control model in the frequency domain. This type of models allow a fast interpretation of the impact of the resonant controllers. However, they neglect some dynamics that can be critical for the grid-forming VSC stability. The simplified control model of the AHF can be found in the Appendix A.

D. Selective Harmonic Overcurrent Protection

The harmonic voltage references $\mathbf{v}^{\star}_{h,\alpha\beta}$ are set to zero by default in order to achieve a perfectly sinusoidal POI voltage. Ideal resonant controllers guarantee null harmonic voltages thanks to the extra harmonic current injection $\mathbf{i}^{\star}_{h,\alpha\beta}$. This, however, may cause VSC overloading if these current terms are not limited. To avoid this situation, it is proposed to add an algebraic virtual harmonic impedance, $Z_h = R_h + jX_h$, which modifies the default harmonic voltage reference in the dq reference frame as:

$$\begin{cases} v^{\star}_{hd} = -R_h i_{sd} + X_h i_{sq}, \\ v^{\star}_{hq} = -X_h i_{sd} - R_h i_{sq}. \end{cases} \tag{21}$$

TABLE I
MAXIMUM AMPLITUDE OF THE HARMONIC VOLTAGES ALLOWED IN THE EN 50160 STANDARD AND VALUE OF THE WEIGHTING FACTORS.

Harmonic order	Amplitude A_h (%)	σ_h (p.u.)
2	2.0	4.0
3, 7	5.0	10.0
4	1.0	2.0
5	6.0	12.0
6, 8, 10, 12	0.5	1.0
9	1.5	3.0
11	3.5	7.0
13	3.0	6.0

The parameters, R_h and X_h, can be independently defined for each targeted *h-th* harmonic, according to the limits imposed in the existing grid code. Larger virtual harmonic impedances can be related to harmonics with higher permissible limits. For doing so, it is proposed to use different harmonic weighting factors, σ_h, to define the virtual harmonic impedances with respect to a base value as:

$$R_h + jX_h = \sigma_h(R_b + jL_b\omega_h), \tag{22}$$

where R_b and L_b represent the base virtual harmonic resistance and inductance respectively. In this way, it is possible to selectively reduce the compensation of each *h-th* harmonic to avoid VSC overcurrents.

Table I defines a set of harmonic weighting factors considering the voltage harmonic limits imposed by the standard EN 50160. Note that the lowest harmonic weighting factor is assigned to the harmonic with the lowest limit, i.e. the sixth harmonic, while the other factors are scaled with respect their relative amplitudes A_h:

$$\sigma_h = \frac{A_h}{A_6} \cdot \sigma_6. \tag{23}$$

The base virtual harmonic impedance is dynamically adapted depending on the VSC current to prevent the overload. Note that, according to (21) and (22), the base virtual harmonic impedance could be computed as a function of the harmonic voltages, harmonic currents and the fundamental current. This work, however, proposes an adaptive approach where the base virtual harmonic impedance is linearly increased whenever the VSC current is greater than its rated current I_{rat}. Considering that the base virtual harmonic impedance is defined as a piece-wise linear function, it is incorporated a hysteresis band $\pm H_{I_s}$ to limit the impedance variations. This band is centered around a current, I_{hys}, below I_{rat}, as shown in Fig. 3. If the POI current, I_s, is lower than I_{rat}, the base virtual harmonic impedance is set to zero, i.e. $\mathbf{v}^{\star}_{h,\alpha\beta} = 0$, being possible to achieve a sinusoidal POI voltage. However, if I_s is greater than I_{rat}, the overcurrent limitation is activated by increasing linearly the base virtual harmonic impedance as:

$$if\ I_s > I_{rat} \rightarrow \begin{cases} R_b(t) = R_b(t-1) + m_r \cdot \Delta t, \\ L_b(t) = L_b(t-1) + m_l \cdot \Delta t, \end{cases} \tag{24}$$

where m_r and m_l are the variation rate of the base virtual harmonic resistance and inductance respectively and Δt is the

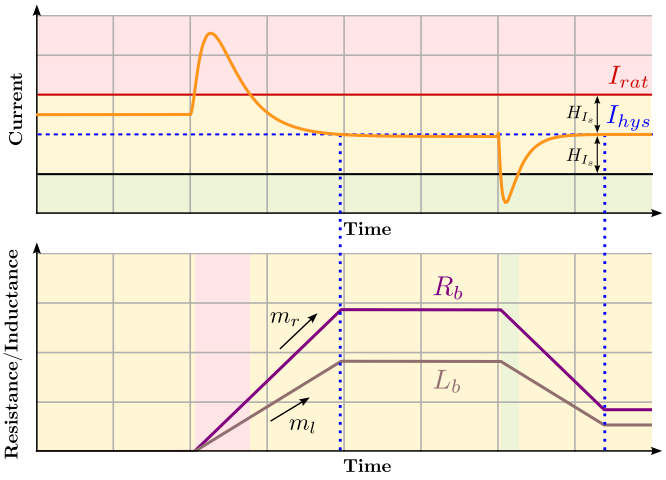

Fig. 3. Overview of the hysteresis band used in the selective overload reduction.

controller sample time. Therefore, the VSC current diminishes, because of the harmonic current reduction, reaching I_{hys}. From this point on, the base virtual harmonic impedance remains constant. As soon as the VSC current drops below the threshold $I_{hys} - H_{I_s}$, the base virtual harmonic impedance is reduced. This leads to an increase of the injected current harmonic currents. If the VSC current reaches I_{hys} and the base virtual harmonic impedance is not null, the VSC current is limited to this value, as shown in Fig. 3. In the case of reaching I_{hys} but with a null base virtual harmonic impedance, it is allowed to increase the VSC current above I_{hys} as long as I_{rat} is not exceeded.

The impact that the components of the base virtual harmonic impedance, R_b and L_b, has on the control algorithm is addressed in section III.

The differential equations of the four previous subsections (1)-(23) can be gathered into a unique state-space model which integrates the system and control dynamics:

$$\begin{cases} \dot{\mathbf{x}} = \mathbf{A}\mathbf{x} + \mathbf{B}\mathbf{u}, \\ \mathbf{x} = [\mathbf{x}_f, \mathbf{x}_{vsg}, \mathbf{x}_h], \\ \mathbf{u} = [p^\star, q^\star, R_b, L_b]. \end{cases} \tag{25}$$

III. Small-Signal Analysis

The aim of this section is to evaluate the stability and dynamic performance of the proposed controller. First, a preliminary computation of the controller gains according to state-of-the-art methods is carried out. Then, the non-linear state-space model of the system presented in the previous section is linearized around an equilibrium point to evaluate their eigenvalues. In addition, the stability range of each control parameter is determined to set the final control gains.

A. Preliminary Computation of the Controller gains

This subsection proposes a preliminary computation of the controller gains shown in Fig. 1:

VSG Outer Control Loop. The active power control loop is based on a PI controller. The integral gain, k_{ip}, is calculated to obtain a given inertial response, while the proportional gain, k_{pp}, is computed depending on the required damping factor. These gains are computed according to [15]:

$$k_{ip} = \frac{1}{2H}; \quad k_{pp} = \sqrt{\frac{8\left(X_v + (L_t + L_s)\omega_0\right)}{3E_0 V_g}} k_{ip}, \tag{26}$$

where H is the inertia constant, V_g is the peak value of the grid voltage, and $X_v = 1/Y_v$ is the virtual reactance. Similarly, the gains of the reactive power control loop are set as [7]:

$$k_{pq} = 0.1\frac{V_g}{S_n}; \quad k_{iq} = 0.1\frac{V_g}{S_n}, \tag{27}$$

where S_n is the rated power of the VSC.

VSG Inner Control Loop. The virtual admittance Y_v is defined as a pure inductive impedance and set to a 10% of the VSC base impedance, whereas the time constant of the LPF, τ_{lpf}, is set to 1.6 ms [7]. The proportional and integral gains of the current control loop are computed according to [44] as:

$$k_{pi} = \frac{L_t + L_s}{\tau_i}; \quad k_{ii} = \frac{R_t + R_s}{\tau_i}, \tag{28}$$

where τ_i is the time constant of the current controller. The value of τ_i is set 10 times higher than the PWM switching period to neglect the PWM dynamics in the design of the current controller.

Active Harmonic Filtering. The resonant gains and the damping term of the resonant controllers are initially calculated according to [45]:

$$\tau_v = \frac{\sqrt{(\tan(M_p - \pi))^2 + 1}}{\omega_c \tan(M_p - \pi)}, \tag{29a}$$

$$k_{rh} = -\frac{C\sum_{h=1}^{n}\left((h\omega)^2 - \omega_c^2\right)}{\tau_v \omega_c \tan(M_p - \pi)}, \tag{29b}$$

where M_p is the phase margin and ω_c is the cutoff filter frequency. These parameters are usually set to $\pi/3$ and a 20% of the maximum compensated harmonic frequency respectively. The base virtual harmonic impedance is initially set to zero for obtaining a full voltage harmonic compensation at the POI.

Table II collects all these controller gains particularized for the system detailed in Table III.

B. Linearization of the State-Space Model

The stability analysis is performed through a small-signal model by linearizing the state-space equations around an equilibrium point $\mathbf{x_0}$. This is obtained by solving (25) for $\dot{\mathbf{x}} = \mathbf{0}$ and a given input vector $\mathbf{u}$. The analysis has been carried out considering the preliminary controller gains, detailed in Table II, computed for a VSC characterized by Table III. The inputs $\mathbf{u}$ have been set for a VSC injected power equal to 9 kW and 4.5 kvar. Regarding the AHF functionality, the targeted harmonics are 5^{th} and 7^{th} harmonics and with a null base virtual harmonic impedance.

The system is linearized as follows:

$$\dot{\mathbf{x}} = \frac{\partial \mathbf{A}}{\partial \mathbf{x}}\Big|_{\mathbf{x_0}} (\mathbf{x} - \mathbf{x_0}), \tag{30}$$

TABLE II
PRELIMINARY, EVALUATED RANGE AND FINAL VALUES OF THE CONTROLLER GAINS.

Parameter	Preliminary	Range	Final	Parameter	Preliminary	Range	Final
H (s)	5	$[0.01,\ 20]$	5	δ_5	10^{-3}	$[0,\ 10^{-3}]$	10^{-3}
k_{pp} ($\frac{rad}{sW}$)	10^{-3}	$[10^{-4},\ 10^{-2}]$	10^{-3}	δ_7	10^{-3}	$[0,\ 10^{-3}]$	10^{-3}
k_{pq} ($\frac{V}{W}$)	0.0016	$[10^{-4},\ 10^{-2}]$	0.0016	k_{r5} ($\frac{A}{V}$)	3.46	$[1,\ 50]$	8
k_{iq} ($\frac{V}{W}$)	0.0016	$[10^{-3},\ 10^{-1}]$	0.016	k_{r7} ($\frac{A}{V}$)	3.46	$[1,\ 50]$	8
G_v (S)	0	$[0, 125]$	0	R_b (Ω)	0	$[0, 0.3]$	0
B_v (S)	1.25	$[0.125, 125]$	1.25	L_b (μH)	0	$[0, 150]$	0
τ_{lpf} (ms)	1.6	$[0.16, 3.2]$	1.6	R_g (Ω)	0.04	$[0, 1]$	0.04
k_{pi} ($\frac{V}{A}$)	5	$[1, 5]$	5	L_g (mH)	0.74	$[0, 2]$	0.74
k_{ii} ($\frac{V}{A}$)	157	$[1.8, 157]$	640				

TABLE III
SYSTEM PARAMETERS USED IN THE STABILITY ANALYSIS AND EXPERIMENTAL VALIDATION.

Parameter	Final	Parameter	Final
L_t (mH)	2.5	R_d (Ω)	28
R_t (Ω)	0.08	V_g (V)	$220\sqrt{2}$
L_s (mH)	2.5	E_0 (V)	$220\sqrt{2}$
R_s (Ω)	0.08	C_f (μF)	1
m_r ($\frac{\Omega}{s}$)	0.025	m_l ($\frac{\Omega}{s}$)	0
σ_2	4	σ_4	2
σ_5	12	σ_7	10
I_{hys} (A)	19	H_{I_s} (A)	1
I_{rat} (A)	20	S_n (kVA)	13
k_{r2} ($\frac{A}{V}$)	4	δ_2	10^{-3}
k_{r4} ($\frac{A}{V}$)	4	δ_4	10^{-3}

TABLE IV
EIGENVALUES OF THE SYSTEM USING THE PRELIMINARY CONTROLLER GAINS.

Eig.	Value	Eig.	Value
λ_1	$-8361.7 - j7711.0\pi$	λ_{12}	$-7959.8 + j7225.6\pi$
λ_2	$-7959.8 - j7225.6\pi$	λ_{13}	$-8361.7 + j7711.0\pi$
λ_3	$-1059.1 - j350.39\pi$	λ_{14}	$-3.1000 - j799.92\pi$
λ_4	$-533.75 - j128.47\pi$	λ_{15}	$-3.6653 - j799.70\pi$
λ_5	$-47.818 - j0.0016\pi$	λ_{16}	$-2.3759 - j599.91\pi$
λ_6	$-31.416 - j0.0002\pi$	λ_{17}	$-2.7529 - j599.60\pi$
λ_7	$-5.8133 - j0.0000$	λ_{18}	$-2.0252 + j399.58\pi$
λ_8	$-0.4388 - j0.0000$	λ_{19}	$-2.1765 + j399.88\pi$
λ_9	$-31.416 + j0.0002\pi$	λ_{20}	$-3.3556 + j599.60\pi$
λ_{10}	$-533.76 + j128.53\pi$	λ_{21}	$-2.9913 + j599.90\pi$
λ_{11}	$-1060.0 + j350.51\pi$		

leading to the small-signal model:

$$\dot{\mathbf{x}} = \mathbf{A_0}\mathbf{x} + \mathbf{B_0}\mathbf{u}. \tag{31}$$

The matrices $\mathbf{A_0}$ and $\mathbf{B_0}$ are the linearized version of $\mathbf{A}$ and $\mathbf{B}$ respectively.

The system stability can be evaluated around the equilibrium point by analyzing the eigenvalues of $\mathbf{A_0}$, which are shown in Table IV for the preliminary values of the controller gains. All the eigenvalues have a non-zero real part, meaning that the system is linearized around an hyperbolic equilibrium point. According to the Hartman-Grobman theorem, the system is structurally stable, so the linearized system faithfully represents the non-linear one in this equilibrium point [46]. It is worth noting that the AHF functionality introduces non-conjugated eigenvalues. Particularly, the 5^{th} harmonic compensation is related to eigenvalues at $+400\pi$ rad/s (λ_{18}, λ_{19}) and -600π rad/s (λ_{16}, λ_{17}). Correspondingly, the 7^{th} harmonic introduces other two eigenvalues at $+600\pi$ rad/s (λ_{20}, λ_{21}) and -800π rad/s (λ_{15}, λ_{16}).

C. Sensitivity Analysis

This subsection evaluates the stability range of the system using the small-signal model and considering the possible variations of the controller gains and the grid impedance. For this purpose, the evolution of the eigenvalues in the complex plane are analyzed when these parameters are modified within the range detailed in Table II. The results are represented using two plots focusing on the eigenvalues of the VSG dynamics, left side, and the AHF functionality, right side, respectively. The arrows within these plots indicate the evolution of the eigenvalues with respect to the analyzed parameter.

VSG active power control loop: The integral gain k_{ip} is inversely proportional to the inertia constant H according to (26). It has been considered that H is within the interval [0.01,20] s, with the results shown in the top left plot of Fig. 4. The system is unstable for very small values of the inertia constant ($H < 1$ s). Larger H stabilizes the system, since the real part of the eigenvalues gets reduced. Therefore, H is adjusted to the required VSC inertial response but greater than 1 s to guarantee the system stability. With respect to the eigenvalues of the AHF, analyzed in the right top plot, these are barely affected by this parameter variation. Regarding the proportional gain k_{pp}, the system stability is compromised if it is increased as shown in the bottom left plot of Fig. 4. This effect is further accentuated from $k_{pp} > 10^{-3}$ rad/(sW) to $k_{pp} = 10^{-3}$, where a drastic damping reduction from 0.8 to an almost null value is noticed in λ_4 and λ_{10}, both related to VSG dynamics. The effect on the AHF eigenvalues is asymmetrical, as depicted in the bottom right plot of Fig. 4. The eigenvalues at negative frequencies are consistently damped, whereas those at positive frequencies get progressively separated from each other approaching to the imaginary axis.

VSG reactive power control loop: The effect of this control loop in the small-signal analysis is usually neglected in the literature as indicated in [47], [48]. Fig. 5, which shows

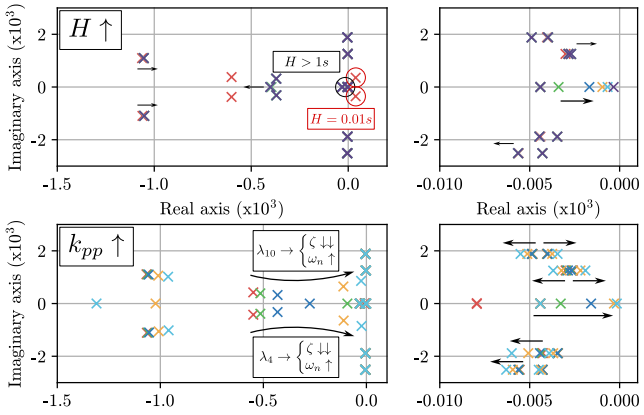

Fig. 4. Evolution of the eigenvalues with respect to the variations of the gains within the active power control loop: $H \in [0.01, 20]$ s and $k_{pp} \in [10^{-4}, 10^{-2}]$.

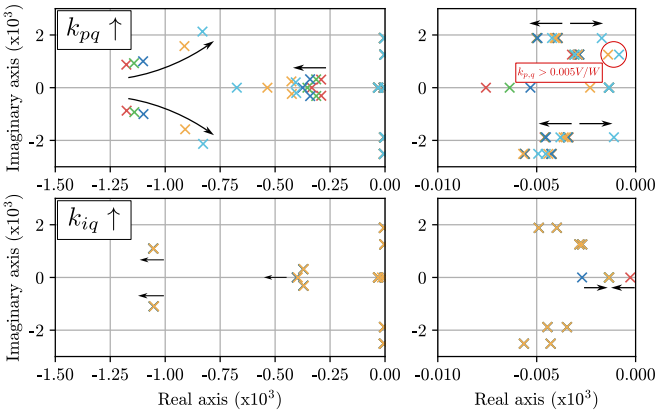

Fig. 5. Evolution of the eigenvalues with respect to the variations of the gains within the reactive power control loop:: $k_{pq} \in [10^{-4}, 10^{-2}]$ V/W and $k_{iq} \in [10^{-3}, 10^{-1}]$ V/W.

the evolution of the eigenvalues as k_{pq} and k_{iq} increase, reinforces this hypothesis. The proportional gain k_{pq} has a relevant impact on eigenvalues as its value increases, but it does not threaten the system stability. Therefore, this gain is selected according to the desired VSC reactive power injection in case of a given POI voltage variation. On the other hand, the integral gain k_{iq} has practically no effect on the dynamics as reflected at the bottom plot of the Fig. 5.

VSG virtual admittance: The effect of the virtual conductance and susceptance are shown in Fig. 6. The virtual conductance G_v has almost no effect on the system dynamics, generating just a slight shift in the eigenvalues as its value increases. In the case of B_v, a slight damping reduction of most of the eigenvalues happens as its value decreases, specially when it is too small. Considering that G_v has almost no impact on the the system dynamics, the virtual admittance is set as purely inductive $Y_v = -jB_v$.

VSG LPF time constant: A LPF time constant equal to zero, i.e. controller without LPF, leads to an unstable system with $\lambda_{2,10} = 472.92 \pm j10889\pi$. The left plot of the Fig. 7 shows that as τ_{lpf} increases the natural frequency of the eigenvalues $\lambda_3, \lambda_4, \lambda_{10}$ and λ_{11} are reduced through a constant-damping path until reaching values only composed of negative real part.

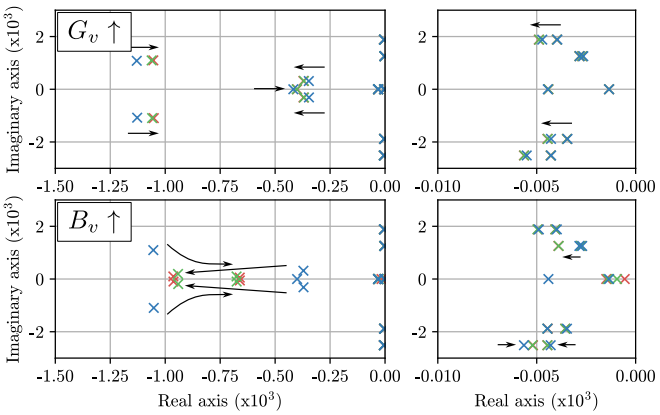

Fig. 6. Evolution of the eigenvalues with respect to the variations the VSG virtual admittance: $G_v = [0, 125]$ S and $B_v \in [0.125, 125]$ S.

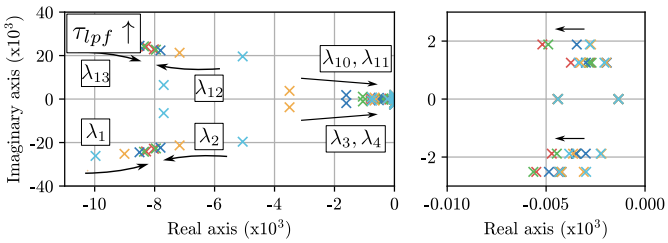

Fig. 7. Evolution of the eigenvalues with respect to the variations of the LPF time constant: $\tau_{lpf} \in [0.16, 3.2]$ ms (bandwith $BW_{lpf} \in [1000, 50]$ Hz).

With respect to eigenvalues λ_2 and λ_{12}, these are shifted to the left increasing the stability of the system. Conversely, the eigenvalues λ_1 and λ_{13} are displaced to the right which can lead to an unstable system. On the other hand, the eigenvalues related to the AHF barely move to the left when the LPF bandwidth decreases. From this analysis, and taking into account that the objective of the LPF is to provide reference currents with the lowest possible harmonic content without affecting too much the dynamics of the current control loop, the LPF time constant is set to $\tau_{lpf} = 1.6$ ms.

VSG current controller: As shown in section III-A, the gains of the PI current controller are limited by the minimum time constant of 1 ms, so the maximum considered values are: $k_{pi} = 5$ and $k_{ii} = 157$. Figure 8 depicts the evolution of the eigenvalues within the ranges of k_{pi} and k_{ii}. The damping of the VSG and AHF increases for large values of k_{pi}. As expected, the wider the PI controller bandwidth the better system performance is obtained. In the case of k_{ii}, its effect is not significant on the system stability. However, this parameter depends on the resistance of the coupling filter as shown in (28). This analysis assumes inductors with a quality factor equal to 10, but it has to be considered that, in practice, the resistance is prone to large variations (manufacturing tolerances, temperature, material degradation, wiring, etc.). For this reason, the final value of k_{ii} is tuned through some experimental tests to obtain a closed-loop time constant of the current controller $\tau_i = 1$ ms.

Active harmonic filtering: As mentioned above, the AHF

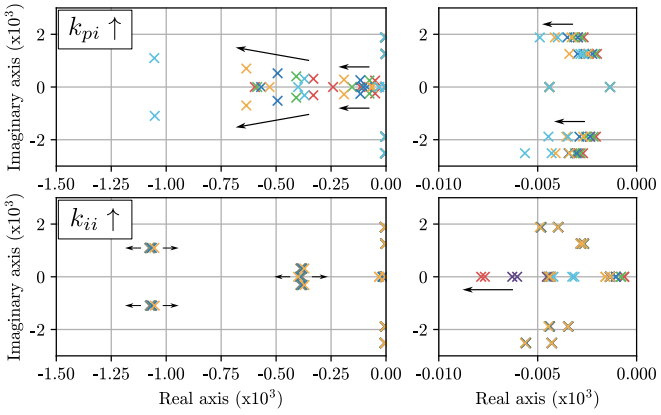

Fig. 8. Evolution of the eigenvalues with respect to the variations of the PI current controller: $k_{pi} \in [1, 5]$ V/A and $k_{ii} \in [1.8, 157]$ V/A.

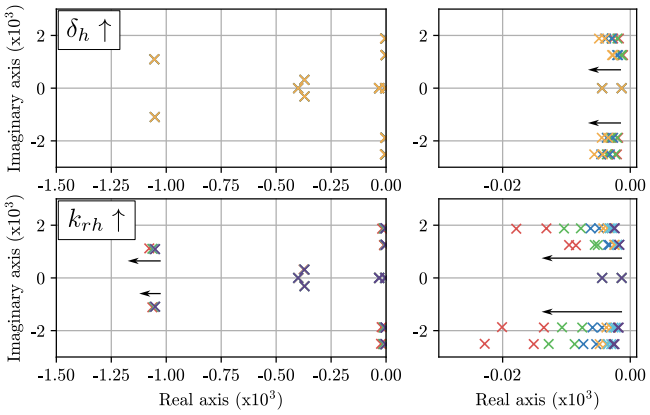

Fig. 9. Evolution of the eigenvalues with respect to the variations of AHF resonant controller: $\delta_h \in [0, 10^{-3}]$ and $k_{rh} \in [1, 50]$ A/V.

functionality is exclusively activated for 5^{th} and 7^{th} harmonics. For the sake of simplicity, it has been considered $k_{r5} = k_{r7} = k_{rh}$ and $\delta_5 = \delta_7 = \delta_h$. The increase of δ_h increases the damping of the AHF functionality, as shown in Fig. 9, compromising the AHF performance but without any effect on the VSG dynamics. With this regard, the best performance is achieved for $\delta_h = 0$ but with the drawback of a limited stability margin which mainly depends on exogenous damping sources. Again, δ_h is a trade-off between providing a large enough AHF capability with enough damping. On the other hand, the resonant gain k_{rh} significantly affects the VSG and AHF dynamics for values higher than 100. Particularly, the natural frequency of the AHF eigenvalues are largely affected, especially those corresponding to the negative sequence. Therefore, it is recommended a low value of k_{rh} with the aim that the AHF capability affects the VSG performance as less as possible. Finally, it is worth noting that the bandwidth of the harmonic voltage controller, involving the cascade operation of the resonant and PI current controllers, is 2931.1 rad/s considering the final values of the controller gains summarized in Table II. This controller bandwidth is enough to mitigate 5^{th} and 7^{th} harmonic voltages without including additional resonant controllers in the VSG current control.

Overcurrent protection: The effect on the stability of the

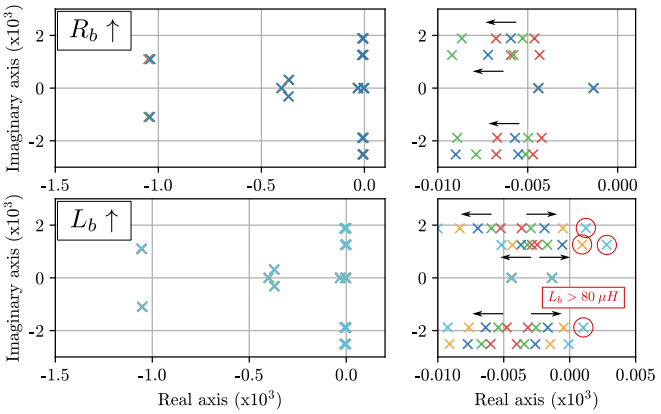

Fig. 10. Evolution of the eigenvalues with respect to the variations of the base virtual harmonic impedance: $R_b \in [0, 0.3]\Omega$ and $L_b \in [0, 0.15]$ mH.

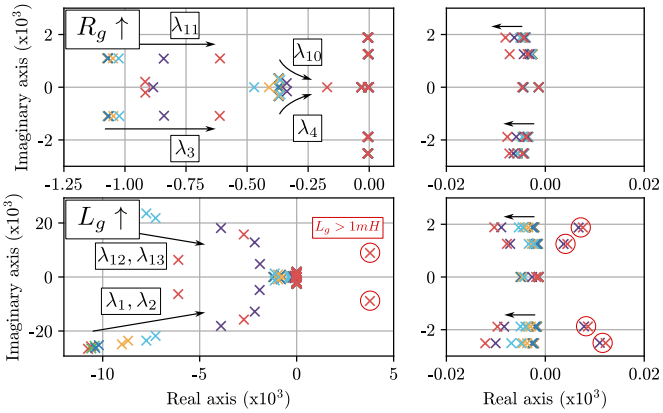

Fig. 11. Evolution of the eigenvalues with respect to the grid impedance: $R_g \in [0, 1]\Omega$ and $L_g \in [0, 1]$ mH.

resistive and inductive terms of the base virtual harmonic impedance are shown in Fig. 10. The VSG eigenvalues are hardly affected, whereas the AHF eigenvalues change differently with respect to the variations of R_b and L_b. The resistance produces a left-side shift of the eigenvalues, increasing the damping. Conversely, the inductive term leads to an unstable system for higher values than $L_b = 80\mu H$. Therefore, it is concluded that the base virtual harmonic impedance must be just resistive.

Grid impedance: The grid impedance has been studied for a wide interval of values of R_g and L_g. The higher the resistance the higher damping of all the eigenvalues. Even with a null value of R_g the system maintains stability. Nevertheless, eigenvalues at average frequencies, λ_3, λ_4, λ_{10} and λ_{11}, tend to move to the right, so it is expected reaching instability for extremely weak grids (e.g. islanded grids). Regarding L_g, the eigenvalues are shifted to the imaginary axis as it is increased. For values higher than 1 mH and a R/X ratio of 0.07 the system becomes unstable.

Considering this sensitivity analysis, the final gains of the controllers used in the experimental validation of the proposed methodology are shown in Table II.

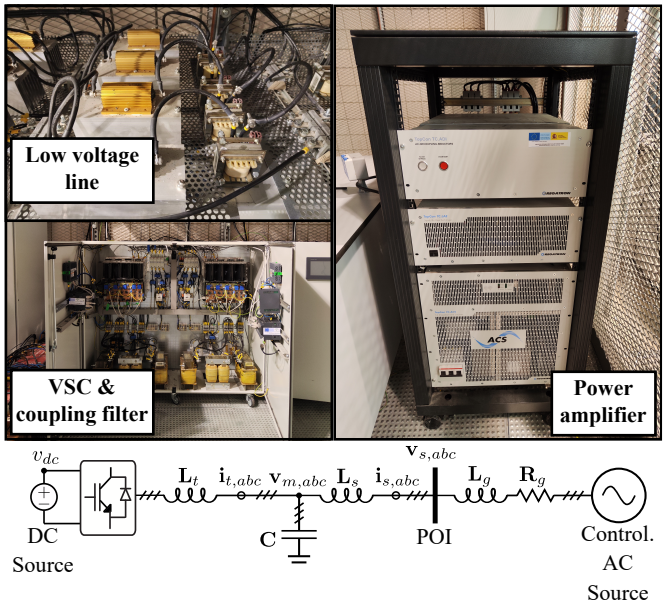

Fig. 12. Main components and one-line diagram of the testbed used for the experimental validation.

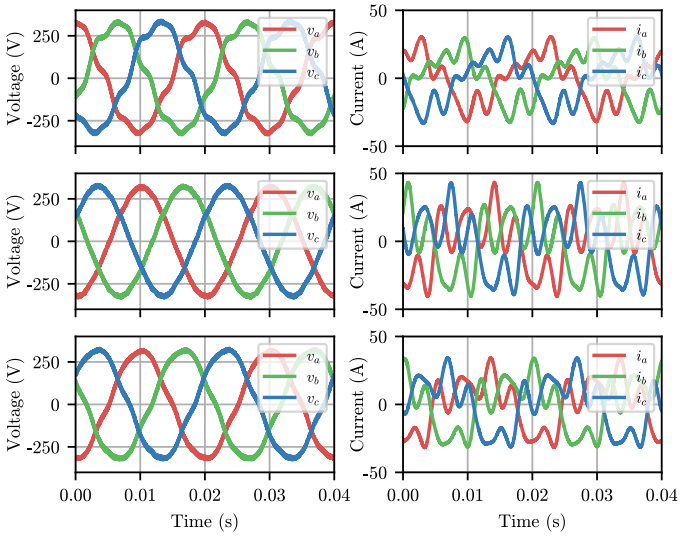

Fig. 13. *Experimental tests*. Steady-state results: Top plot: *Test 1*, no AHF is provided. Middle plot: *Test 2*, AHF is activated. Bottom plot: *Test 3*, AHF is activated with overload protection ($R_b = 0.0942\,\Omega$).

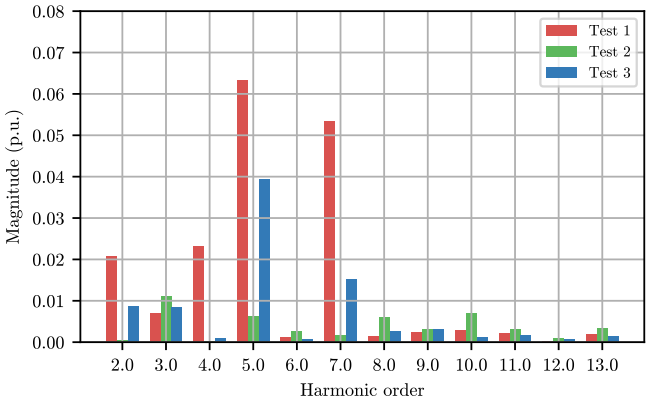

Fig. 14. *Experimental tests*. Steady-state results: FFT of the voltages. *Test 1*, no AHF is provided. *Test 2*, AHF is activated. *Test 3*, AHF is activated with overload protection ($R_b = 0.0942\,\Omega$).

IV. Experimental Validation

The experimental validation of the grid-forming VSC including AHF with overload protection has been carried out using a testbed with the one-line diagram shown at the bottom of Fig. 12. This consists of a three-phase three-wire VSC with a DC voltage source and connected through an LCL filter to a low-voltage power grid. This grid is composed of a controllable power source, being possible to add voltage harmonics, and a series impedance. The controller gains and relevant parameters of this experimental testbed are summarized in the Table II and Table III respectively. The AHF is exclusively activated for compensating the 2^{th}, 4^{th}, 5^{th} and 7^{th} harmonics. The experimental validation has been done through steady-state and dynamic tests which are summarized in the next subsections.

A. Steady-state Test Results

The AC controllable source has been adjusted to supply a fundamental phase-to-neutral voltage of 220 V distorted with the following harmonics: $U_2 = 6.9$ V, $U_4 = 2.3$ V, $U_5 = 22.7$ V and $U_7 = 13.5$ V. The active and reactive power references of the grid-forming VSC have been set to 9 kW and 4.5 kvar. Using this testbed configuration, three different VSC modes have been tested:

- *Test 1* (T1). No voltage harmonic compensation is applied.
- *Test 2* (T2). The AHF capability for the 2^{nd}, 4^{th}, 5^{th} and 7^{th} harmonics is activated but without overloading protection.
- *Test 3* (T3). The AHF functionality is enabled including the proposed selective overload protection.

The instantaneous VSC voltages and currents, $\mathbf{v}_{s,abc}$ and $\mathbf{i}_{s,abc}$, for these steady-state tests are shown in Fig. 13, whereas their corresponding harmonic spectrum for the targeted harmonics is detailed in Fig. 14 and Table V.

Test 1 is characterized by highly distorted POI voltages which lead to distorted currents, since the current controller uses the POI voltage to track the power references. Note that the VSC current, I_s, is below its rated value, I_{rat}, since *Test 1* is only focused on supplying the active and reactive power reference without any harmonic compensation.

Test 2 evidences a remarkable improvement of the POI voltage as shown in the middle plot of Fig. 13, Fig. 14 and Table V. Note that the 2^{nd}, 4^{th}, 5^{th} and 7^{th} harmonic voltages are almost null and the THD_V is reduced below a 2%. Furthermore, it is relevant to note these low THD_V evidences that the rest of harmonic frequencies have not been excited by the use of the harmonic resonant controllers. This harmonic voltage improvement, however, is achieved at the cost of a high VSC harmonic current which leads to the VSC overload (106.05%).

TABLE V
STEADY-STATE TESTS RESULTS: THD, 2^{nd}, 4^{th}, 5^{th}, 7^{th} HARMONICS, VSC TOTAL CURRENT AND FUNDAMENTAL ACTIVE AND REACTIVE POWERS.

Test	*T1*	*T2*	*T3*
THD_V [%]	8.88	1.76	4.42
V_2 [%]	2.08	0.03	0.87
V_4 [%]	2.31	0.03	0.10
V_5 [%]	6.32	0.63	3.94
V_7 [%]	5.33	0.15	1.51
THD_I [%]	15.16	45.80	15.33
I_2 [%]	17.18	43.52	32.29
I_4 [%]	16.22	9.00	7.04
I_5 [%]	26.07	81.31	52.51
I_7 [%]	25.01	33.66	24.41
I_{RMS} [A]	16.51	21.21	18.83

This situation can be fully prevented implementing the proposed AHF functionality with selective overload protection, evaluated in *Test 3*. With this regard, the POI voltage is more distorted than this of *Test 2*, since the AHF controller increases the harmonic voltage references with the aim of limiting the harmonic current injection. For doing so, the virtual harmonic base impedance is dynamically adjusted to limit the harmonic current, reaching a final value of $R_b = 0.0942\Omega$. Furthermore, the selective harmonic limitation using σ_h is noticed by comparing the harmonic voltages of *Test 2* and *Test 3* in Table V and Fig. 14. Since the standard allows a greater 5^{th} harmonic content, the AHF functionality imposes a higher reduction of the 5^{th} harmonic current injection compared to the other targeted harmonics.

B. Dynamic Test Results

The purpose of this test is to show the dynamic performance of the proposed AHF with selective overload protection. This dynamic test has been done by modifying the harmonic voltages of the programmable AC source: from 4.6 V to 6.9 V for the 2^{nd} harmonic, from 1.2 V to 2.3 V for the 4^{th} harmonic, from 16.1 V to 22.7 V for the 5^{th} harmonic and from 9.2 V to 13.5 V for the 7^{th} harmonic at $t = 7.5$ s and returning to the original values at $t = 17.5$ s. The active and reactive VSC power references are set to 9 kW and 4.5 kvar, which lead to scenario below the VSC rated current at the beginning of the test. In this situation, the POI voltage harmonics are almost null, as shown in the top plot of Fig. 15, thanks to the injection of VSC harmonic currents. Due to the change of the source harmonic voltages at $t = 7.5$ s, the AHF functionality provides additional current harmonic injection to reduce the POI voltage harmonics, as shown in the two top plots of Fig. 15. As a result, the VSC current overpasses its rated value and the selective overload protection is activated by increasing the base virtual harmonic resistance as depicted in the second to last plot of Fig. 15. This linear increase is stopped when the current reaches the current I_{hys}, set to 19 A, as previously explained with the help of Fig. 3 and the base virtual harmonic resistance remains constant up to $t = 17.5$ s. At this instant, the sudden reduction of the POI voltage harmonics leads to a reduction of the VSC current which overpasses the lower limit

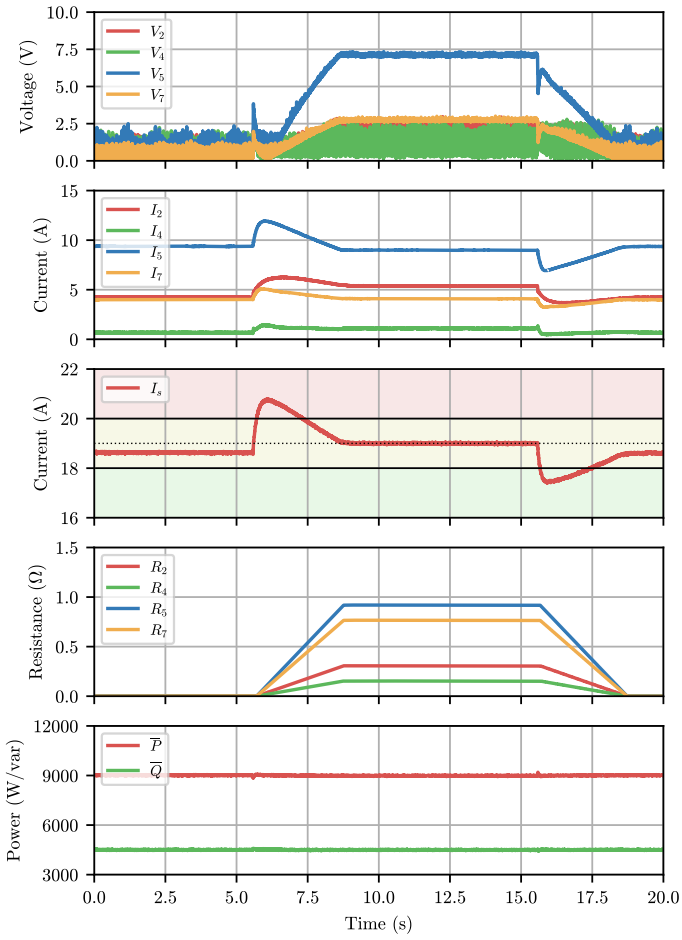

Fig. 15. *Experimental tests.* From top to bottom: Harmonic voltages, harmonic currents, RMS current I_s, evolution of the virtual harmonic resistances and active and reactive power for the fundamental component during the dynamic test.

of the hysteresis band, $I_{hys} - H_{I_s}$. Therefore, the base virtual harmonic resistance starts decreasing up to zero since the VSC current remains below I_{hys}. Finally, the bottom plot of Fig. 15 shows the evolution of the average active and reactive powers throughout the test. It is observed that these remains constant in the setpoints regardless of the activation or deactivation of the AHF selective overcurrent protection. This reflects that limiting the provision of AHF to avoid VSC overcurrent does not affect other functionalities such as the provision of active and reactive power.

V. CONCLUSION

This paper has presented a selective current limitation strategy to regulate the AHF capability of grid-forming VSCs to prevent overload conditions. A harmonic voltage reference, obtained as a function of the injected VSC current and a virtual harmonic impedance, is fed to a set of resonant controllers tuned to the targeted harmonic frequencies. The output of these resonant controllers is added to the reference current of the VSG current control loop. The value of the virtual harmonic impedance for each harmonic is selected according to its relative importance within the existing power quality

standard, e.g. EN 50160. This allows to prioritize the reduction of the VSC harmonic currents in overload conditions.

A sensitivity analysis based on the small-signal model of the state-space equations has been done to evaluate the dynamic performance and stability of the controller as well as the influence of each controller gain. This analysis reflects that the tuning of the proportional gain in the VSG active power control loop, the proportional gain of the PI current controller, the LPF of the current controller and the virtual harmonic reactance in the overload protection is key to achieve an stable system. As a matter of fact, this analysis reveals that the suppression of the LPF and the use of the virtual harmonic reactance may lead to system instability. Furthermore, this analysis has evidenced that the proposed VSG with AHF functionality is stable for a wide range of grid impedances.

The proposal has been validated in a laboratory testbed through test cases dealing with steady-state and dynamic conditions. The steady-state results show that the controller is able to eliminate the targeted harmonic components within the resonant controllers. In addition, the controller shows a good dynamic response in transient conditions when sudden changes in the grid harmonic voltages take place. With respect to VSC overload situations, the virtual harmonic impedance strategy has demonstrated to be an efficient methodology to maintain the VSC currents within the permissible technical limits without affecting the other functionalities of the grid-forming VSC.

Future research lines will involve the analysis of unbalanced scenarios with three-phase four-wire VSCs. In addition, this local control strategy can be complemented with another centralized or distributed controller in charge of optimizing globally some network variable like harmonic distortion, imbalance or power losses.

ACKNOWLEDGMENTS

This work was supported by Grant PID2021-124571OB-I00 funded by MCIN/AEI/ 10.13039/501100011033, by "ERDF A way of making Europe" and the European Union under the H2020 project EASY-RES (GA 764090).

REFERENCES

[1] X. Liang, "Emerging Power Quality Challenges Due to Integration of Renewable Energy Sources," *IEEE Transactions on Industry Applications*, vol. 53, pp. 855–866, mar 2017.

[2] D. Liu, X. Zhang, and C. K. Tse, "Effects of high level of penetration of renewable energy sources on cascading failure of modern power systems," *IEEE Journal on Emerging and Selected Topics in Circuits and Systems*, vol. 12, no. 1, pp. 98–106, 2022.

[3] A. Huda and R. Živanović, "Large-scale integration of distributed generation into distribution networks: Study objectives, review of models and computational tools," *Renewable and Sustainable Energy Reviews*, vol. 76, pp. 974–988, 09 2017.

[4] D. Kumar and F. Zare, "Harmonic Analysis of Grid Connected Power Electronic Systems in Low Voltage Distribution Networks," *IEEE Journal of Emerging and Selected Topics in Power Electronics*, vol. 4, pp. 70–79, 03 2016.

[5] A. B. Nassif, "Assessing the Impact of Harmonics and Interharmonics of Top and Mudpump Variable Frequency Drives in Drilling Rigs," *IEEE Transactions on Industry Applications*, vol. 55, no. 6, pp. 5574–5583, 2019.

[6] R. Rosso, X. Wang, M. Liserre, X. Lu, and S. Engelken, "Grid-Forming Converters: Control Approaches, Grid-Synchronization, and Future Trends—A Review," *IEEE Open Journal of Industry Applications*, vol. 2, no. May, pp. 93–109, 2021.

[7] G. C. Kryonidis, J. M. Mauricio, K. N. D. Malamaki, M. Barragán-Villarejo, F. de Paula García-López, F. J. Matas-Díaz, J. M. Maza-Ortega, and C. S. Demoulias, "Use of ultracapacitor for provision of inertial response in virtual synchronous generator: Design and experimental validation," *Electric Power Systems Research*, vol. 223, no. March, p. 109607, 2023.

[8] T. Qoria, T. Prevost, G. Denis, F. Gruson, F. Colas, and X. Guillaud, "Power converters classification and characterization in power transmission systems," *2019 21st European Conference on Power Electronics and Applications, EPE 2019 ECCE Europe*, pp. P.1–P.9, 2019.

[9] J. Rocabert, A. Luna, F. Blaabjerg, and P. Rodríguez, "Control of power converters in AC microgrids," *IEEE Transactions on Power Electronics*, vol. 27, no. 11, pp. 4734–4749, 2012.

[10] P. Rodríguez, C. Citro, J. I. Candela, J. Rocabert, and A. Luna, "Flexible grid connection and islanding of spc-based pv power converters," *IEEE Transactions on Industry Applications*, vol. 54, no. 3, pp. 2690–2702, 2018.

[11] B. B. Johnson, S. V. Dhople, A. O. Hamadeh, and P. T. Krein, "Synchronization of parallel single-phase inverters with virtual oscillator control," *IEEE Transactions on Power Electronics*, vol. 29, no. 11, pp. 6124–6138, 2014.

[12] Q. Lei, F. Z. Peng, and S. Yang, "Multiloop control method for high-performance microgrid inverter through load voltage and current decoupling with only output voltage feedback," *IEEE Transactions on Power Electronics*, vol. 26, no. 3, pp. 953–960, 2011.

[13] C. Li, Y. Yang, Y. Cao, L. Wang, and F. Blaabjerg, "Frequency and voltage stability analysis of grid-forming virtual synchronous generator attached to weak grid," *IEEE Journal of Emerging and Selected Topics in Power Electronics*, vol. 10, no. 3, pp. 2662–2671, 2022.

[14] P. Rodriguez, I. Candela, C. Citro, J. Rocabert, and A. Luna, "Control of grid-connected power converters based on a virtual admittance control loop," *2013 15th European Conference on Power Electronics and Applications, EPE 2013*, pp. 1–10, 2013.

[15] G. C. Kryonidis, K.-N. D. Malamaki, J. M. Mauricio, and C. S. Demoulias, "A new perspective on the synchronverter model," *International Journal of Electrical Power & Energy Systems*, vol. 140, p. 108072, 2022.

[16] J. C. Olives-Camps, J. M. Mauricio, M. Barragán-Villarejo, and F. J. Matas-Díaz, "Voltage control of four-leg vsc for power system applications with nonlinear and unbalanced loads," *IEEE Transactions on Energy Conversion*, vol. 35, no. 2, pp. 640–650, 2020.

[17] F. J. Matas-Díaz, M. Barragán-Villarejo, J. C. Olives-Camps, J. M. Mauricio, and J. M. Maza-Ortega, "Virtual conductance based cascade voltage controller for vscs in islanded operation mode," *Journal of Modern Power Systems and Clean Energy*, vol. 10, no. 6, pp. 1704–1713, 2022.

[18] M. H. Ravanji, D. B. Rathnayake, M. Z. Mansour, and B. Bahrani, "Impact of Voltage-Loop Feedforward Terms on the Stability of Grid-Forming Inverters and Remedial Actions," *IEEE Transactions on Energy Conversion*, no. March, 2023.

[19] N.-B. Lai, G. Baltas, and P. Rodriguez, "Small-signal modeling of grid-forming power converter," in *2022 IEEE 13th International Symposium on Power Electronics for Distributed Generation Systems (PEDG)*, pp. 1–5, 06 2022.

[20] A. T. Pereira and H. Pinheiro, "Inner loop controllers for grid-forming converters," in *2022 14th Seminar on Power Electronics and Control (SEPOC)*, pp. 1–6, 2022.

[21] A. Narula, P. Imgart, M. Bongiorno, M. Beza, J. R. Svensson, and J.-P. Hasler, "Voltage-based current limitation strategy to preserve grid-forming properties under severe grid disturbances," *IEEE Open Journal of Power Electronics*, vol. 4, pp. 176–188, 2023.

[22] J. C. Churio-Barboza and J. M. Maza-Ortega, "Comprehensive design methodology of tuned passive filters based on a probabilistic approach," *IET Generation, Transmission & Distribution*, vol. 8, no. 1, pp. 170–177, 2014.

[23] M. El-Habrouk, M. Darwish, and P. Mehta, "Active power filters: A review," *IEE Proceedings - Electric Power Applications*, vol. 147, pp. 403–413(10), September 2000.

[24] X. Liang and C. Andalib Bin-Karim, "Harmonics and mitigation techniques through advanced control in grid-connected renewable energy sources: A review," *IEEE Transactions on Industry Applications*, vol. 54, no. 4, pp. 3100–3111, 2018.

[25] N. Pogaku and T. Green, "Harmonic mitigation throughout a distribution system: a distributed-generator-based solution," *IEE Proceedings-Generation, Transmission and ...*, vol. 151, no. 3, pp. 201–212, 2004.

[26] A. Micallef, M. Apap, C. Spiteri-Staines, and J. M. Guerrero, "Mitigation of Harmonics in Grid-Connected and Islanded Microgrids Via Virtual Admittances and Impedances," *IEEE Transactions on Smart Grid*, vol. 8, no. 2, pp. 651–661, 2017.

[27] M. Barragán-Villarejo, J. M. Mauricio, J. C. Olives-Camps, F. J. Matas-Díaz, F. de Paula García-López, and J. M. Maza-Ortega, "Harmonic and imbalance compensation in grid-forming vsc," in *2020 IEEE International Conference on Industrial Technology (ICIT)*, pp. 757–762, 2020.

[28] A. Micallef, M. Apap, C. Spiteri-Staines, and J. M. Guerrero, "Selective virtual capacitive impedance loop for harmonic voltage compensation in islanded microgrids," in *IECON 2013 - 39th Annual Conference of the IEEE Industrial Electronics Society*, pp. 7968–7973, 2013.

[29] C. A. Rojas, S. Kouro, R. Inzunza, Y. Mitsugi, and A. M. Alcaide, "Harmonic impedance model of multiple utility-interactive multilevel photovoltaic inverters," *Energies*, vol. 15, no. 24, 2022.

[30] V. Salis, A. Costabeber, S. M. Cox, and P. Zanchetta, "Stability assessment of power-converter-based ac systems by ltp theory: Eigenvalue analysis and harmonic impedance estimation," *IEEE Journal of Emerging and Selected Topics in Power Electronics*, vol. 5, no. 4, pp. 1513–1525, 2017.

[31] X. Wang and F. Blaabjerg, "Harmonic Stability in Power Electronic-Based Power Systems: Concept, Modeling, and Analysis," *IEEE Transactions on Smart Grid*, vol. 10, no. 3, pp. 2858–2870, 2019.

[32] B. Fan, X. Wang, and S. Member, "Current-Limiting Control of Grid-Forming Inverters: State-of-the-Current-Limiting Control of Grid-Forming Inverters: State-of-the-Art and Open Issues Art and Open Issues," pp. 1–9.

[33] E. Afshari, G. R. Moradi, R. Rahimi, B. Farhangi, Y. Yang, F. Blaabjerg, and S. Farhangi, "Control strategy for three-phase grid-connected pv inverters enabling current limitation under unbalanced faults," *IEEE Transactions on Industrial Electronics*, vol. 64, no. 11, pp. 8908–8918, 2017.

[34] L. Zhou, S. Liu, Y. Chen, W. Yi, S. Wang, X. Zhou, W. Wu, J. Zhou, C. Xiao, and A. Liu, "Harmonic current and inrush fault current coordinated suppression method for vsg under non-ideal grid condition," *IEEE Transactions on Power Electronics*, vol. 36, no. 1, pp. 1030–1042, 2021.

[35] G. Denis, T. Prevost, M.-S. Debry, F. Xavier, X. Guillaud, and A. Menze, "The migrate project: the challenges of operating a transmission grid with only inverter-based generation. a grid-forming control improvement with transient current-limiting control," *IET Renewable Power Generation*, vol. 12, pp. 523–529(6), April 2018.

[36] T. Liu, X. Wang, F. Liu, K. Xin, and Y. Liu, "A current limiting method for single-loop voltage-magnitude controlled grid-forming converters during symmetrical faults," *IEEE Transactions on Power Electronics*, vol. 37, no. 4, pp. 4751–4763, 2022.

[37] A. G. Yepes and J. Doval-Gandoy, "Effective current limitation for multifrequency current control with distortion-free voltage saturation and antiwindup," *IEEE Transactions on Power Electronics*, vol. 35, no. 12, pp. 13697–13713, 2020.

[38] J. Paulo Bonaldo, F. Lessa Tofoli, R. Vitor Arantes Monteiro, and H. Kelis Morales-Paredes, "Comparative analysis of techniques for the limitation of compensation currents in multifunctional grid-tied inverters," *International Journal of Electrical Power & Energy Systems*, vol. 126, p. 106574, 2021.

[39] G. Abad, A. Laka, G. Saavedra, and J. A. Barrena, "Analytical modeling approach to study harmonic mitigation in ac grids with active impedance at selective frequencies," *Energies*, vol. 11, no. 6, 2018.

[40] M. A. Ebrahim, B. A. Aziz, M. N. Nashed, and F. Osman, "Optimal design of controllers and harmonic compensators for three-level cascaded control in stationary reference frame for grid-supporting inverters-based ac microgrid," *Energy Reports*, vol. 8, pp. 860–877, 2022.

[41] F. J. Matas-Díaz, M. Barragán-Villarejo, J. M. Maza-Ortega, G. C. Kryonidis, K.-N. Malamaki, and C. S. Demoulias, "Active harmonic filtering of islanded converter interfaced generation considering the thermal limits," in *2022 International Conference on Smart Energy Systems and Technologies (SEST)*, pp. 1–6, 2022.

[42] "DIN EN 50160:2020-11 — Normas AENOR."

[43] Y. Li, Y. Xia, Y. Ni, Y. Peng, and Q. Feng, "Transient Stability Analysis for Grid-Forming VSCs Based on Nonlinear Decoupling Method," *Sustainability (Switzerland)*, vol. 15, no. 15, 2023.

[44] A. Yazdani and R. Iravani, *Voltage-sourced converters in power systems: modeling, control, and applications*. IEEE Press/John Wiley, 2010.

[45] M. Barragan-Villarejo, J. M. Mauricio, J. C. Olives-Camps, F. J. Matas-Diaz, F. De Paula Garcia-Lopez, and J. M. Maza-Ortega, "Harmonic and imbalance compensation in grid-forming VSC," *Proceedings of the IEEE International Conference on Industrial Technology*, vol. 2020-Febru, pp. 757–762, 2020.

[46] L. Baratchart, M. Chyba, and J.-B. Pomet, "On the differentiability of feedback linearization and the hartman-grobman theorem for control systems," in *Proceedings of the 38th IEEE Conference on Decision and Control (Cat. No.99CH36304)*, vol. 2, pp. 1617–1622 vol.2, 1999.

[47] W. Wu, Y. Chen, L. Zhou, A. Luo, X. Zhou, Z. He, L. Yang, Z. Xie, J. Liu, and M. Zhang, "Sequence impedance modeling and stability comparative analysis of voltage-controlled vsgs and current-controlled vsgs," *IEEE Transactions on Industrial Electronics*, vol. 66, no. 8, pp. 6460–6472, 2019.

[48] Y. Peng, Y. Wang, Y. Liu, P. Yu, S. Shu, and W. Lei, "A full sequence impedance modelling and stability analysis of the virtual synchronous generator with inner loops," *IET Renewable Power Generation*, vol. 15, no. 2, pp. 397–408, 2021.

Francisco Jesús Matas-Díaz was born in Spain in 1995. He received the aerospace engineering degree and the Master degree in power systems from the University of Seville, Seville, Spain, in 2017 and 2020 respectively, where he is currently a research assistant at the Department of Electrical Engineering. His primary research interests involve the control of power converters and the provision of ancillary services related to power quality, as well as HIL testing and experimental validation of power converters.

Manuel Barragán-Villarejo was born in Marmolejo, Spain, in 1984. He received the Electrical Engineering and Ph.D. degrees in electrical engineering from the University of Seville, Seville, Spain, in 2008 and 2014, respectively. Since 2008, he has been with the Department of Electrical Engineering, University of Seville, where he is currently an Assistant Professor. His primary research interests include exploitation and control of power converters for smart grid management and grid integration of distributed renewable energy sources.

José María Maza-Ortega received the Electrical Engineering and Ph.D. degrees from the University of Seville, Spain, in 1996 and 2001, respectively. Since 1997, he has been with the Department of Electrical Engineering, University of Seville, where he is currently a Full Professor. His primary areas of interest are power quality, harmonic filters, integration of renewable energies and power electronics.

Georgios C. Kryonidis received the Dipl.Eng. and Ph.D. degrees from the School of Electrical and Computer Engineering, Aristotle University of Thessaloniki, Greece, in 2013 and 2018, respectively. Currently, he is an PostDoctoral Researcher at the same University. His research interests include distributed generation and storage, renewable energy sources, microgrids, and smart grids operation and control.

Kyriaki-Nefeli Malamaki received the Dipl. and Ph.D. degrees in electrical and computer engineering from the Department of Electrical and Computer Engineering (DECE) at Aristotle University of Thessaloniki (AUTH), Greece, in 2012 and 2020, respectively. Currently, she is a Post-doctoral Researcher at the DECE, AUTH. Her research interests include distributed generation and storage, power quality,

interface of renewable energy sources with the grid, power electronic converters control and their integration within the smart grid context.

Charis S. Demoulias received the Diploma and Ph.D. degree in electrical engineering from the Aristotle University of Thessaloniki, Thessaloniki, Greece, in 1984 and 1991, respectively. He is currently an Associate Professor with the Electrical Machines Laboratory, Department of Electrical and Computer Engineering, Aristotle University of Thessaloniki. His research interests include the fields of power electronics, harmonics, electric motion systems, and renewable energy sources.

APPENDIX
SIMPLIFIED MODEL OF THE AHF FUNCTIONALITY

The simplified model of the AHF functionality based on transfer functions using the nomenclature of Fig. 1 is represented in Fig. A1. The terms $R(s)$ and $PI(s)$ represent the transfer functions of the resonant controller within the harmonic voltage controller and the PI controller of the current control loop respectively:

$$R(s) = \frac{k_{rh}s}{s^2 + 2\delta_h\omega_h s + \omega_h^2},$$

$$PI(s) = \frac{k_{pi}s + k_{ii}}{s}.$$

The rest of the terms represents the different impedances and admittances of the system $Z_t = L_t s + R_t$, $Z_s = L_s s + R_s$, $Y_m = C_f s + G_d$, $Z_g = L_g s + R_g$. Note that the VSG dynamics has been neglected, i.e. $G_{inv}(s) = 1$, since its much faster than the analyzed AHF and current control loops. Therefore, the open-loop transfer function $G_{OL}(s)$ of this model can be computed as:

$$G_{OL}(s)|_{v_g=0} = \frac{e_{vs}}{v_s} = \frac{G_{inv}(s)PI(s)R(s)}{Z_t Y_m Z_p + Z_e + G_{inv}(s)PI(s)}$$

where $Z_p = Z_s + Z_g$ and $Z_e = Z_t + Z_s + Z_g$.

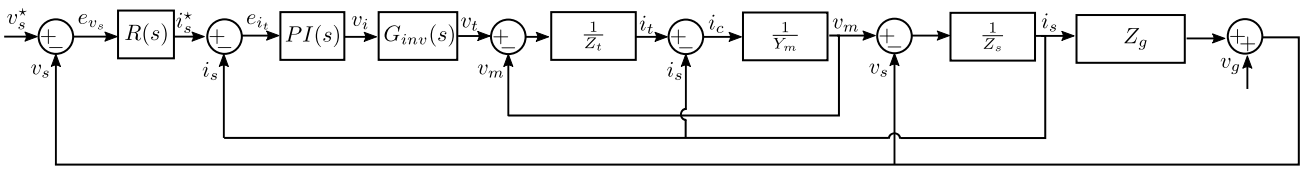

Fig. A1. Transfer function representation of the AHF functionality.

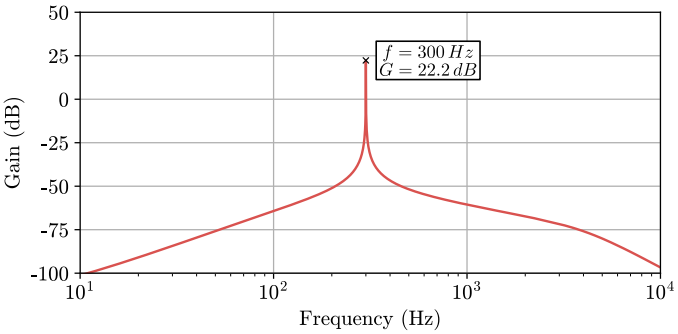

Fig. A2. Bode plot of the magnitude for the $G_{OL}(s)$ of the system.

The Bode diagram related to $G_{OL}(s)$ is shown in Fig. A2 particularized with the final controller gains and parameters of Table II and Table III respectively. Note that the AHF functionality has been applied just to the 6^{th} harmonic, which represents the negative sequence of the 5^{th} harmonic and the positive sequence of the 7^{th} harmonic in the dq domain. As reflected in the Bode diagram, the peak magnitude is located at 300 Hz (6^{th} harmonic) while the rest of frequencies have a magnitude lower than -50dB. This means that the AHF functionality only acts on the 6^{th} harmonic without affecting to the rest of frequencies of the system. This result is consistent with the experimental results depicted in Fig. 14, where only the harmonics tuned at the resonant controllers are mitigated without affecting the rest of frequencies.